IEEE Access
Multidisciplinary | Rapid Review | Open Access Journal

Received July 30, 2019, accepted August 20, 2019, date of publication August 27, 2019, date of current version September 11, 2019.

Digital Object Identifier 10.1109/ACCESS.2019.2937729

Hyperspectral Push-Broom Microscope Development and Characterization

SAMUEL ORTEGA, RAÚL GUERRA, MARÍA DÍAZ, HIMAR FABELO, SEBASTIÁN LÓPEZ, (Senior Member, IEEE), GUSTAVO M. CALLICÓ, (Member, IEEE), AND ROBERTO SARMIENTO

Institute for Applied Microelectronics (IUMA), University of Las Palmas de Gran Canaria (ULPGC), 35017 Las Palmas de Gran Canaria, Spain

Corresponding author: Samuel Ortega (sortega@iuma.ulpgc.es)

This work was supported in part by the Canary Islands Government through the "Agencia Canaria de Investigación, Innovación y Sociedad de la Información (ACIISI)" (Canarian Agency for Research, Innovation and the Information Society), ITHACA Project "Hyperspectral Identification of Brain Tumours" under Grant ProID2017010164, and in part by the Ministry of Economy and Competitiveness (MINECO) of the Spanish Government (PLATINO) under Project TEC2017-86722-C4-1-R. The work of S. Ortega and M. Díaz was supported by Pre-Doctoral Grant given by the "Agencia Canaria de Investigación, Innovación y Sociedad de la Información (ACIISI)" of the "Conserjería de Economía, Industria, Comercio y Conocimiento" of the "Gobierno de Canaria," which is part-financed by the European Social Fund (FSE) under Grant POC 2014-2020, Eje 3 Tema Prioritario 74 (85%).

ABSTRACT Currently, the use of hyperspectral imaging (HSI) for the inspection of microscopic samples is an emerging trend in different fields. The use of push-broom hyperspectral (HS) cameras against other HSI technologies is motivated by their high spectral resolution and their capabilities to exploit spectral ranges beyond 1000 nm. Nevertheless, using push-broom cameras in miscroscopes imposes to perform an accurate spatial scanning of the sample to collect the HS data. In this manuscript, we present a methodology to correctly set-up a push-broom HS microscope to acquire high-quality HS images. Firstly, we describe a custom 3D printed mechanical system developed to perform the spatial scanning by producing a precise linear movement of the microscope stage. Then, we discuss how the dynamic range maximisation, the focusing, the alignment and the adequate speed determination affect the overall quality of the images. Finally, we present some examples of HS data showing the most common defects that usually appear when capturing HS images using a push-broom camera, and also a set of images acquired from real microscopic samples.

INDEX TERMS Hyperspectral imaging, microscopy, system analysis and design, data acquisition, image analysis, image enhancement.

I. INTRODUCTION

In the last decades, hyperspectral imaging (HSI) has become a very popular emerging technique employed in numerous areas and applications. This kind of images collects information along the whole electromagnetic spectrum, covering a wide range of wavelengths which generally span the visible, near-infrared and mid-infrared portions of the spectrum. On this basis, hyperspectral (HS) images can be seen as a three-dimensional (3D) data structure where two dimensions correspond to spatial information while the third dimension stands for the spectral information. Unlike traditional panchromatic and multispectral images, HS images show a high spectral resolution, permitting to collect information of very narrow and continuous spectral bands. Since all materials reflect, absorb or emit electromagnetic energy at specific wavelengths, this characteristic of the HS images permits to reconstruct the radiance spectrum of every image pixel and consequently, to identify different materials on the basis of their spectral shape. This property makes HS data beneficial for many applications such as vegetation and water resource monitoring [1], non-invasive sensing of food-quality [2], geology [3], diagnosis of multiple cancers [4]–[8], among-others.

In general, HS imaging has been more commonly applied to remote sensing applications [9], [10]. However, the use of HSI for microscopic examination of samples has recently attracted the attention of many researchers from different

The associate editor coordinating the review of this article and approving it for publication was Huimin Lu.

fields [11]. In mineralogy, *Pirad et al* used HS microscopic images for the quantitative analysis of minerals [12], finding strong correlation between the collected spectral signatures and previously collected spectrographic data. *Jaap van der Weerd et al*. applied this methodology to identify and classify different pigments in paint cross sections obtained from paintings, exploiting the potential of the visible spectra in the detection process [13]. Furthermore, this technology was used to evaluate the disease resistant of plants to different pathogens in smart farming applications [14], [15].

However, it is in the medical field where HS microscopic imaging has emerged as a potential tool for non-invasive disease diagnosis [16]. Many clinical diagnosis of different diseases are usually carried out by HS microscopic examination of histological samples. For this reason, the use of new imaging technologies as aid-tools is increasing in this field. In [17], a microscope-based HSI system is used for the studio of hemoglobin saturation in tumor microvasculature and tumor hypoxia development. *Siddiqi et al.* analysed the suitability of HS images for distinguishing normal, precancerous, and cancerous cells to reduce the mortality from cervical cancer [18]. *Maggioni et al.* applied HS microscopic analysis to classify normal, benign adenoma and malignant carcinoma colon biopsies [19].

Although HSI technology has shown great potential in a wide variety of applications, one of the biggest challenges in HSI is that the instrumentation is not standardized. There are several types of HS acquisition systems, being the main difference among them the method employed to generate an HS cube. Besides, there are three main features that describe any HS system: the *spectral range*, the *spectral resolution* and the *spatial resolution*. The *spectral range* is the portion of the electromagnetic spectrum sampled by an HS camera. There are several standard values for the spectral range in commercial HS systems. The term Visible and Near-Infrared (VNIR) is used for the spectral range from 400 to 1000 nm, while Near-Infrared (NIR) and Short Wave Infrared (SWIR) refer to the ranges 1000-1700 nm and 1000-2500 nm, respectively. The *spectral resolution* refers to the maximum number of spectral bands that can be resolved by an HS camera, while the *spatial resolution* is defined as the size of the smallest object that can be recorded by the camera. The successful information retrieval from each application demands fixed specifications of HS systems, and these requirements in terms of spectral range, spectral resolution and spatial resolution are not known beforehand.

The most widely used methods to acquire HS images are based on staring or spectral-scanning instruments, which capture the whole scene in a band-sequential format, and push-broom scanners, which generate the HS cube in a line-by-line fashion [16]. Staring array systems have limited spectral resolution due to a low number of spectral filters, which makes them not suitable for research applications. In these cases, push-broom scanners stand as a very competitive alternative which offers high spectral resolution with very reasonable spatial resolution. Furthermore, the spectral range of spectral-scanning system is limited to the VNIR and NIR spectral ranges. For these reasons, push-broom systems are adequate to evaluate which spectral range and spectral bands are relevant for a given application. However, their use in HS microscopic applications is very limited due to the high complexity to ensure high resolution movements and an accurate spatial scanning, specially with high magnifications. Only a few publications about HS push-broom microscopic systems can be found in the literature [20]–[24].

This work is presented as a solution to the limitations imposed by the push-broom scanners to be properly combined with HS microscope imaging system. To do this, we present a customized microscope with HS capabilities as well as a general methodology to correctly couple a HS push-broom camera to a microscope to capture high quality HS images. On this basis, this manuscript is organized as follows. In Section II, the key concepts related with HS acquisition systems are reviewed, highlighting how each element of the instrumentation influences the overall system response. In Section III, the proposed customized microscope HSI system is presented. In Section IV, the proposed methodology to correctly set up a push-broom microscope to capture high-quality HS data is explained in detail. Section V displays different representations of real HS data collected using the described acquisition system. Finally, Section VI presents the conclusions drawn from this work.

II. HYPERSPECTRAL/MULTISPECTRAL INSTRUMENTATION

In this section, we provide a brief description of HS systems and we discuss how each element of the instrumentation affects to the *spectral response*, the *spatial resolution* and the *dynamic range* of the acquisition system.

There are three key elements in every HS acquisition system: a lens, an electronic sensor and a light source. The lens is intended to focus the scene, while the sensor records the HS data. The light is devoted to illuminate the scene. Depending on the HS technology, a fourth element will perform the electromagnetic spectrum sampling. On the one hand, spectral-scanning systems make use of an optical element that filters the incoming light at discrete wavelengths, being able to collect the whole spatial information for such wavelength. The central wavelength of such optical filters can be tuned both mechanically (filter wheels) or electronically (Acousto-Optic Tunable Filters and Liquid Crystal Tunable Filters) to generate an HS cube. On the other hand, push-broom systems make use of optical grating elements able to perform the diffraction of light across a narrow line. In this sense, the complete spectral dimension and a single spatial dimension are captured simultaneously. In order to obtain an HS cube, push-broom systems require to perform a spatial scanning across the remaining spatial dimension. In this sense, the complete spectral dimension and a single spatial dimension are captured simultaneously. In order to obtain an HS cube, push-broom systems require to perform a spatial scanning across the remaining spatial dimension.

Each element of the acquisition system contributes to its overall *spectral response*. Firstly, the sensor that samples the information has an intrinsic spectral response due to its quantum efficiency, which is wavelength-dependent. In conventional greyscale or RGB (Red, Green and Blue) high-performance imaging systems, Silicon-based sensors are widely employed. Nevertheless, Silicon shows poor sensitivity above 1100 nm. For this reason, other detectors have to be used for measurements beyond the infra-red (IR) range of the spectrum. In HS imagery, the most common semiconductors used to record data within the IR are Indium Gallium Arsenide (InGaAs) or Mercury Cadmium Telluride (MCT), which are sensitive up to 2500 nm approximately [25]. Although this type of sensors are used to record the IR spectrum, they present some drawbacks such as a limited number of pixels and higher shot noise than Silicon-based sensors. Due to this reason, cooling systems are typically coupled to HS sensors to alleviate such noise. Secondly, light transmission through the lens is also wavelength-dependent. For this reason, specific lens with fixed transmission spectra have to be used in order to avoid spectral losses [26]. Finally, the overall spectral response of the HS acquisition setup relies on spectral shape of the light source. Typically halogen or Xenon-based light sources are employed to this end [27].

In addition, the *spatial resolution* is influenced by both the lens and the sensor. On the one hand, the optical properties of the lens determine the Field of View (FOV) of the optical system, which is usually expressed as an angle. Furthermore, the size of the final image depends of the distance between the lens and the object to be captured. Besides the FOV, the optical properties of the lens also limit the size of the minimum object that can be captured, i.e. the resolving power of the lens. On the other hand, the number of pixels that the sensor is able to acquire will determine the spatial resolution of the overall acquisition system. While Silicon sensors are characterized by high pixel density, other sensor technologies (such as InGaAs or MCT) are restricted to a lower pixel density. This means that IR measurements (above 1000 nm) are restricted in the sensor size, worsening the spatial resolution in such spectral range. Besides, in push-broom systems the spatial resolution in the scanning direction is ultimately determined by the mechanical resolution of the linear movement mechanism that performs the scan.

Finally, the *dynamic range* is defined as the difference between the maximum and the minimum values that bounds the measurements capabilities of an instrument [28]. In this context, the dynamic range of an HS camera is determined by the radiometric resolution of the sensor, i.e. it is directly related to the number of bits used for the image registration. Nevertheless, in an HS acquisition system the maximization of the dynamic range does not exclusively depend on the bit depth of the sensor. The light measured by the sensor depends on two main factors: the power of the incoming light and the exposure time. The illumination power may be constrained by each application, existing situations where is not possible to just increase the light power to maximize the effective dynamic range of a measurement. The exposure time (also known as the *integration period*) is the fraction of time that the sensor collects light. For this reason, the quantity of light measured by the sensor is ultimately determined by the integration time.

For the previously mentioned reasons, HS images are highly biased by both the instrumentation and the environmental conditions. In order to remove the influence of the acquisition system in the measurements, a *calibration* procedure is usually followed. The calibration of HS images will be covered latter in this manuscript.

A. SOME NOTIONS ABOUT PUSH-BROOM MEASUREMENTS

As mentioned before, push-broom cameras are able to acquire a 2-D frame containing both the spatial and the spectral information of a narrow line across the lens FOV. An appropriate visualization and interpretation of push-broom frames (namely Y-lambda image) are important for an intuitive usage and configuration of push-broom cameras. Y-lambda images are commonly used for focusing push-broom HS cameras. In addition, Y-lambda images can be used to set up the optimal illumination level for a given application. The visualization of Y-lambda images can reveal, among others, non-homogeneous distribution of light across the FOV or the spectral distribution of the light source.

In this paper, we make an extensive use of Y-lambda images, so we provide some insights about such images. A Y-lambda image is a conventional 2-D grayscale image, where the Y-axis represents the spectral dimension, the X-axis represents the spatial dimension and the gray level indicates the luminance at a certain pixel. Usually, the first rows of the image are associated to the lowest wavelengths, and the latter ones to the highest wavelengths. For a certain pixel, its value represents the measured luminance at a certain wavelength in a certain position across the spatial dimension. If we extract a single column (fixed X position) from a Y-lambda image, it is possible to visualize the spectra of a certain pixel within the X-axis, while a single row represents the spatial distribution for a fixed wavelength.

In Fig. 1 we present a toy example to visually clarify some concepts regarding Y-lambda images. To this end, we select a sample contained in a slide, where there is only a single black dot printed on its center. A graphical representation of the HS cube of this toy example is shown in Fig. 1.a, while its spatial shape is shown in Fig. 1.b. Within the sample, we represent three different push-broom lines, namely P_1, P_2 and P_3. P_1 is located in a blank part of the slide, while P_2 and P_3 are sections that cross different parts of the black dot.

In Fig. 1c-1e we represent the Y-lambda images associated to P_1, P_2 and P_3. Some conclusions can be extracted directly from the Y-lambda image, such as the presence of objects within the FOV, or some intuitions about the illumination conditions. Nevertheless, to correctly exploit the information within a Y-lambda image, we can visualize the spatial and the spectral information separately. First, the visualiza-

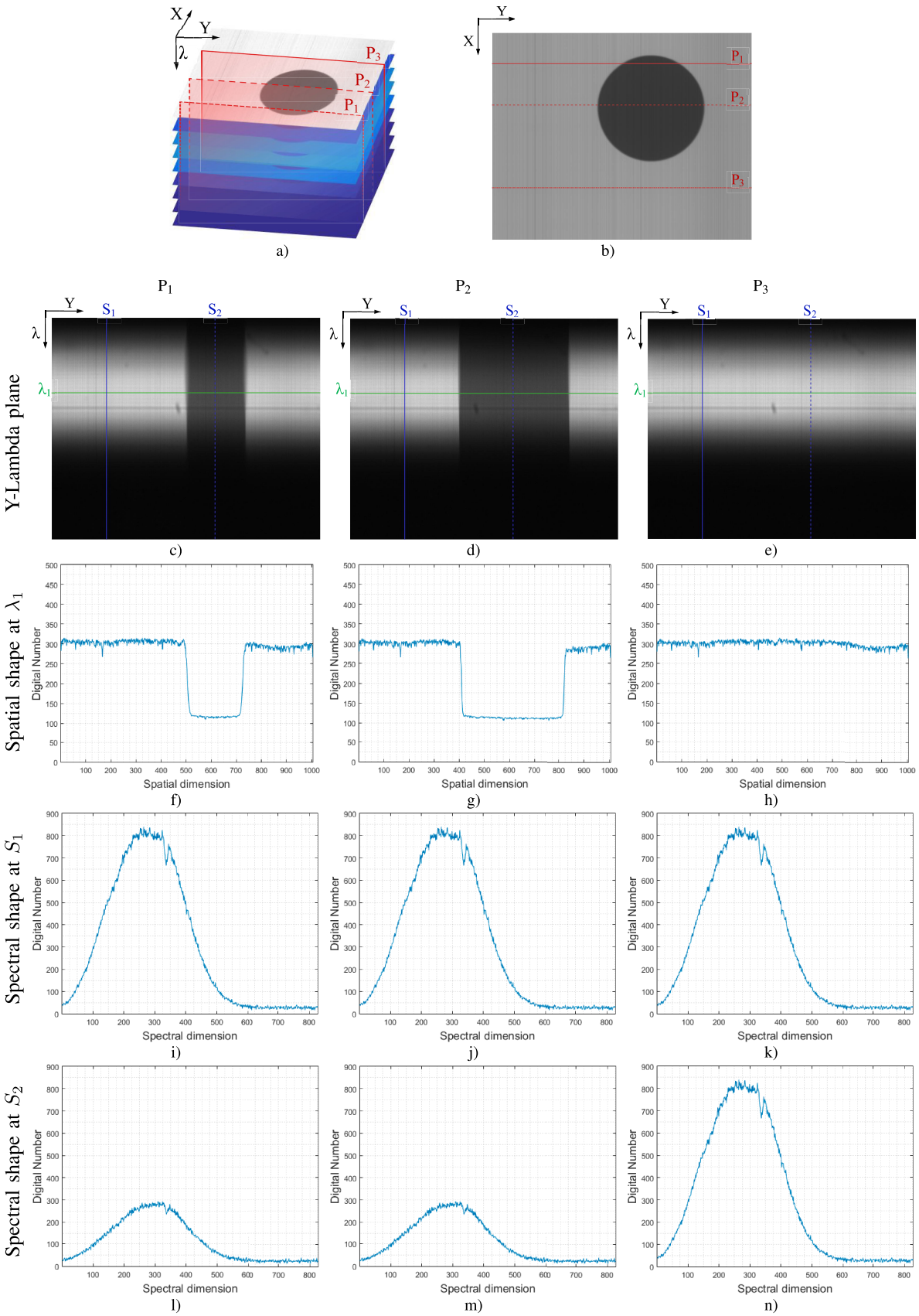

FIGURE 1. Y-lambda image a) HS cube b) Spatial distribution of the HC and spatial location of different *P* planes, c)-e) Y-lambda planes for P_1, P_2 and P_3, f)-h) Spatial profiles at λ_1, i)-k) Spectral profiles at S_1, l)-n) Spectral profiles at S_2.

tion of the spatial information of a given scene within the Y-lambda image requires the selection of a fixed wavelength. This spatial information can be extracted from the Y-lambda image by selecting a discrete row (λ_1 in Fig. 1c-1e). The corresponding spatial profile for such spectral channel can be extracted as the pixel value of all the columns for such row. In Fig. 1f, 1g and 1h, we can visualize the spatial profile of P_1, P_2 and P_3, respectively. For P_3, where there is no sample, the spatial profile is flat, showing high luminance values for the entire FOV. On the contrary, the P_2 and P_3 counterpart show low luminance values in the center of the spatial profile, corresponding to the presence of the black dot within the FOV. The visualization of such spatial profiles is extensively used for focusing HS push-broom cameras. Secondly, to visualize the spectral information we have to select a spatial position. Within the Y-lambda images represented in Fig. 1c, 1d and 1e, we chosen two different spatial points, namely S_1 and S_2, located in a blank part of the scene and inside the black dot respectively (blue lines in the figure). If we represent the rows corresponding to such spatial locations, we retrieve their spectral shape (Fig. 1i-1n). On the one hand, we can observe the spectral shape of the blank part of the scene in Fig. 1i-1k and 1n, which represent the spectral shape of the light source used in the toy example. On the other hand, in Fig. 1l and 1m the spectral shape of the black dot is represented, showing low transmittance values in all wavelengths.

III. MATERIALS AND METHODS

The instrumentation employed in this study is composed by two main parts: the optical subsystem and the mechanical subsystem (Fig. 2). The optical subsystem is composed by both the microscope optic path and a push-broom HS camera. The mechanical subsystem is mainly devoted to perform the spatial scanning in the push-broom acquisition subsystem. This mechanical subsystem is composed by a custom 3D printed transmission mechanism, an stepper motor and a controller. Furthermore, an additional custom 3D printed mechanism is included, which allows to perform an accurate positioning of the HS camera relative to the microscope. Further details about this acquisition system are depicted in this section.

A. OPTICAL SUBSYSTEM

The optical subsystem employed in our system consists of an HS camera coupled to a conventional light microscope. The microscope is an Olympus BH2-MJLT (Olympus, Tokyo, Japan). The main features of this microscope are the dual illumination mode, which allows the observation both in transmittance and reflectance; the trinocular (BH2-TR3), permits the attachment of a camera with a selectable light path (i.e. is able to bring the light into the observation eyepieces, to the camera or to both of them); the objective lenses, that are from the Neo S Plan family (Olympus, Tokyio, Japan) with five different magnifications: 5x, 10x, 20x, 50x and 100x. The microscope also provides an in-house illumination system based on a 12 V - 50 W halogen lamp.

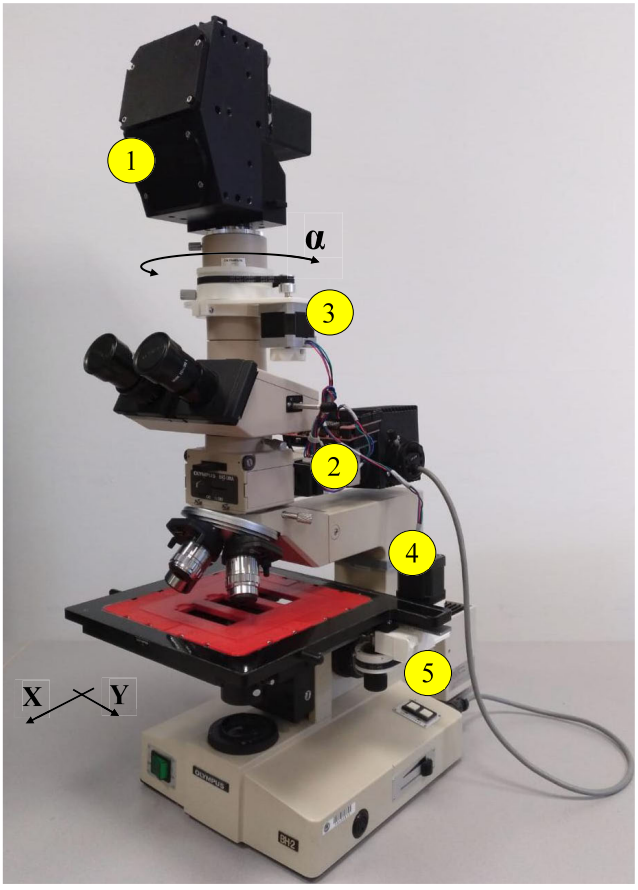

FIGURE 2. Acquisition System. 1) VNIR HS camera. 2) Controller of the mechanical system. 3) Camera alignment mechanism. 4) Stepper motor for controlling the sample movement. 5) Custom 3D printed transmission mechanism.

The HS camera is directly coupled to the microscope using the Olympus MTV-3 C-mount adapter. The MTV-3 adapter includes a 0.3x relay lens. In order to project the image from the trinocular to the MTV-3, a special lens for microphotography is used. In our setup, this lens is the NFK 3.3 LD (Olympus, Tokyo, Japan) and it is devoted to maximize the area covered by the camera attached to the trinocular and hence, makes this area closer to the one observed through the trinocular eyepieces.

The push-broom HS camera is a Hyperspec©VNIR A-Series from HeadWall Photonics (Fitchburg, MA, USA), which is based on a imaging spectrometer coupled to a CCD (Charge-Coupled Device) sensor, the Adimec-1000m (Adimec, Eindhoven, Netherlands). This HS system works in the spectral range from 400 to 1000 nm (VNIR) with a spectral resolution of 2.8 nm, being able to sample 826 spectral channels and 1004 spatial pixels.

The FOV captured by the camera will depend on both the lens magnification (M_i) and the sensor size of the camera (S_s), as shown in (1). The sensor size can be calculated as the product of the pixel size of the sensor (P_s) by its number of pixels (N). For this camera, the pixel size is 7.4 μm, while the overall magnification of the optical system is determined by

the magnification of each lens, the 0.3x relay lens and the 3.3x from the microphotography lens. This means that the overall magnification of the system is about 0.99 the lens magnification. Using this information, we are able to calculate the FOV for the different magnifications. The theoretical FOV is 1.5 mm, 750.45 μm, 375.23 μm and 148.59 μm for the 5x, 10x, 20x and 50x magnifications respectively.

$$FOV = \frac{P_s \cdot N}{M_i} = \frac{S_s}{M_i} \tag{1}$$

B. MECHANICAL SUBSYSTEM

A relative motion between the HS sensor and the targeted sample is needed in order to acquire HS data cubes using a sensor based on a push-broom scanner. The quality and limitations of the acquired images are strongly related to the characteristics of this relative movement. Due to this reason, a high effort has been made in this work in order to achieve good movement conditions according to the goals of the application at hand.

In our particular acquisition system, the HS sensor remains motionless, placed over the microscope, while the sample to be scanned is moved taking advantage of the microscope moving system. By default, the movement system of the microscope is manual, in which two knobs can be manually rotated for moving the sample in the X and Y directions using two rack and pinion gears mechanisms. A stepper motor has been set up for driving the handle corresponding to the X direction. By doing so, the movement in the X direction has been automated, which can be controlled from the computer in order to synchronize the sample movement with the sensor acquisition process. The stepper motor is controlled using a DRV8825 driver plugged into an Arduino UNO board, which communicates with the computer through the USB serial port. The stepper motor has been mechanically fixed using a custom designed 3D printed mechanism that includes a pulley transmission and a planetary reduction, as it can be seen in Fig. 3. The main goal of this mechanism is to fulfill the mechanical requirements imposed by the application at hand.

In the acquisition process followed in this work, the HS push-broom sensor is continuously capturing frames while the sample to be scanned is moving in the X direction according to the motor steps. Two important mechanical restrictions must be fulfilled in order to acquire high quality images using this kind of acquisition process. First of all, the resolution of the mechanical movement system must be considerably higher than the optical resolution. That is, the smaller distance that the sample can be moved has to be considerably smaller than the pixel size. In this way, the mechanical movement of the sample is perceived as a continuous and uniform displacement by the scanning sensor. On the contrary, if the smaller distance that the sample can be moved is close to the pixel size, the scanning sensor perceives the movement as a sequence of jumps that correspond with the motor steps. Needless to say that if the smaller distance that the sample

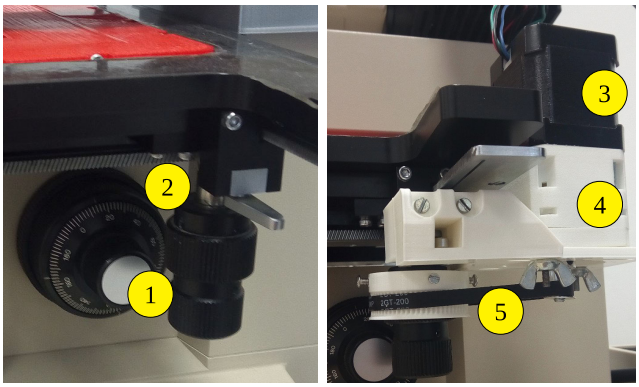

FIGURE 3. Mechanism made of custom designed 3D printed parts for automatically moving the samples in the X direction. 1: Microscope handles for manual movements. 2: Microscope rack and pinion gear mechanism. 3: Stepper motor. 4: Planetary reduction. 5: Pulley reduction.

can be moved is larger than the pixel size, there will be gaps between subsequent acquired frames. Secondly, the stepper motor rotation speed has to be not too high, nor too low, so it can efficiently work, avoiding vibrations and overheating. The required motor rotation speed depends on the mechanical resolution and the linear speed at which the sample has to be moved. This linear speed depends on the optical resolution and the frame rate at which the sensor is capturing the data, as it is further explained in Section IV-F.

Generally, the linear movement of the sample is proportional to the movement of the stepper motor, multiplied by the transmission ratio of the system (TR_{system}), as shown in (2) and (3), where D_{linear} refers to the linear distance that the sample is moved for each motor step, and S_{linear} is the linear speed at which the sample is moved according to the rotation speed of the motor ($S_{rotation}$) measured in steps per second. $MSPR$ refers to the number of steps per motor revolution.

$$D_{linear} = TR_{system} \cdot \frac{1}{MSPR} \tag{2}$$

$$S_{linear} = TR_{system} \cdot \frac{1}{MSPR} \cdot S_{rotation} \tag{3}$$

Whereas we are targeting a microscopic application and the aforementioned mechanical requirements for acquisition systems based on push-broom sensors has to be fulfilled, the project at hand needs a mechanical system able to accurately move very short distances and at a very low but continuous and uniform speed. Hence, according to (2) and (3), a small TR_{system} value is desired, as well as a high $MSPR$. In particular, the selected stepper motor has 400 steps per revolution. Additionally, the DRV8825 driver is able to increase the stepper motor steps per revolution by introducing micro-steps up to a maximum of 32 micro-steps per motor steps. Accordingly, the minimum $MSPR$ for our motor is 400 steps per revolution and the maximum is 12800 steps per revolution ($400 \cdot 32$).

The TR_{system} can be depicted as shown in (4), where $TR_{planetary}$ refers to the transmission ratio of the planetary reduction placed after the motor, TR_{pulley} refers to the

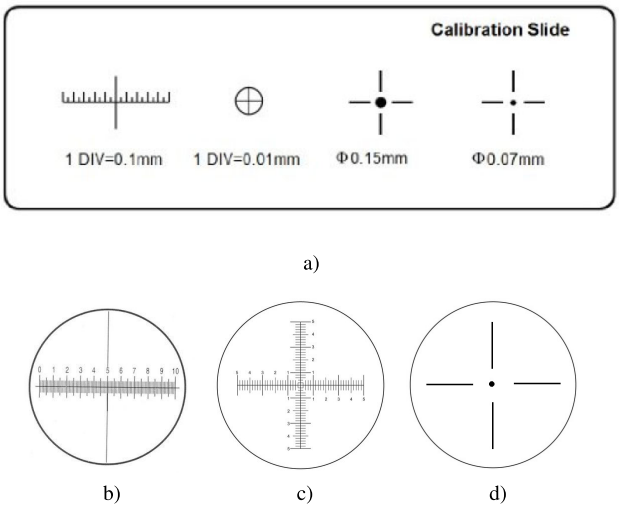

FIGURE 4. Calibration slide. a) Complete calibration slide. b) Micrometer scale, with 0.1 mm divisions. c) Two-axis micrometer scale, with 0.01 mm divisions and d) Black dot, 0.07 and 0.15 mm diameter.

transmission ratio of the pulley reduction placed between the planetary reduction and the microscope handle, and TR_{gear} refers to the transmission ratio of the microscope rack and pinion gear mechanism, measured in millimeters per revolution. The transmission values that corresponds to the custom designed 3D printed parts are $TR_{planetary} = 1/5$ and $TR_{pulley} = 16/64$. The transmission ratio of the rack and pinion gear mechanism is 42 millimeters per revolution (28 teeth with a pitch of 1.5 millimeters). This results in a considerably small transmission ratio ($TR_{system} = 2.1$ mm per revolution (rv)). Additionally, more than one planetary reduction can be stacked together for obtaining extra 1/5 reductions.

$$TR_{system} = TR_{planetary} \cdot TR_{pulley} \cdot TR_{gear}$$
$$TR_{system} = \frac{1}{5} \cdot \frac{16}{64} \cdot 42 = 2.1 \frac{mm}{rv} \quad (4)$$

According to these values, the mechanical resolution of the system is 164.0625 nm per motor step. This means that the minimal distance that the sample can be moved is $D_{linear} = 0.1640625\ \mu$m.

C. CALIBRATION INSTRUMENTATION

In our methodology for setting up an HS push-broom microscope, we employ a microscope calibration slide (Fig. 4) composed by four different parts: a single axis micrometer scale, a dual axis micrometer scale and two dots with different diameter. The single axis micrometer scale has a length of 10 mm with divisions of 0.1 mm, numbered from 10 to 1. The dual axis scale ranges in 0.01 mm each division, having also additional markers which facilitates measurements of 0.05 mm. Finally, the diameter of the target dots are 0.15 and 0.07 mm respectively.

IV. METHODOLOGY

In this section, we present a methodology to correctly set up an HS push-broom microscope to capture high quality HS images. This methodology involves the set up of the light conditions, the optical focusing of the system, the camera alignment, and the empirical measurement of both the FOV and the mechanical resolution of the scanning platform. Additionally, a methodology for quantitatively verifying the correct set up of the whole system is described. Finally, we show the most common defects that may appear when the system is not properly configured.

A. DYNAMIC RANGE CHARACTERIZATION OF THE HSI SYSTEM

The first step prior to capture an HS cube is the configuration of the illumination conditions. There are three main factors that should be taken into account for light adjustment of HS cameras: the spectral shape of the light source, the light intensity and the spatial distribution of light across the camera's FOV. First, an optimal light source for HSI should ideally present a flat spectral response along the spectral range of the camera. If there is no radiation of light in some regions of the spectral range of the camera, it will be impossible to acquire images in such spectral bands. The spectrum emitted by the light source depends on the type of illumination. Second, normally it is desirable to maximize the light intensity measured by the camera, i.e. maximizing the dynamic range. There are two ways to maximize the dynamic range in HS measurements: increasing either the exposure time or the illumination intensity. On the one hand, the exposure time adjustment can improve the dynamic range conditions, but at the expenses of increasing the time required to collect an HS cube. The exposure time can be also limited by the hardware itself, i.e. the maximum and minimum exposure time will strongly depend on sensor manufacturers. On the other hand, variations in light source power can improve the exploitation of dynamic range, but light illumination adjustment is not possible in some situations. There is a trade-off between acquisition time, dynamic range and the available illumination conditions.

For the reasons discussed above, to properly characterize the illumination conditions of an HS instrumentation, we should pay special attention to the spectral shape of the light source, the light intensity and the spatial distribution of light across the FOV. In our acquisition system, the illumination is provided by the in-house 50 W halogen lamp of the microscope, and the maximum exposure time that can be configured in the camera is 40 ms. The first configuration of the system was just observing the microscope light (with no sample) using the highest light power provided by the in-house lighting and also the highest exposure time supported by the camera. To fully characterize the illumination conditions, we analyzed an Y-lambda image. In order to observe both the measured spectral shape and the dynamic range exploitation, we analyzed the mean spectral profile of the Y-lambda image (Fig. 5a) using the 4 different magnifications available. By visual inspection, it is possible to notice that the spectral shape of the measured light is not flat. These spectra are mostly influenced by the spectra of

the light source, the spectral transmission response of the microscope light path and the spectral response of the sensor. Attending to Fig. 5a, it is possible to notice that, although the spectral range of the HS camera covers from 400 to 1000 nm, the instrumentation limits the effective spectral range to approximately 400-800 nm.

To visualize the spatial distribution of light in our system, we analyze a spatial profile from the Y-lambda image. In Fig. 5b, we show the spatial illumination conditions of our system, where a flat response can be observed for each objective lens.

Fig. 5 also shows that the full dynamic range of the acquisition system is not maximized, even with the maximum light power and exposure time. Furthermore, it can be observed that each objective lens present different transmission losses, being the higher magnifications the ones which present higher attenuation of light. In the herein setup, the only way to improve the dynamic range usage of our system is by attaching an external high-power light source. The improvement of the dynamic range conditions is mandatory to acquire HS images with high magnification. Due to the poor light intensity captured when using the 50x objective lens, the experiments in this paper are limited to the 5x, 10x and 20x magnifications.

Finally, we performed an additional experiment to illustrate the effect of varying the exposure time. Fig. 5c shows that the best dynamic range exploitation is achieved when the higher exposure time is selected.

B. FOCUSING AN HS IMAGE

Focusing targets are usually employed for focusing both conventional and HS cameras. Using an appropriate focusing target, the acquisition system is considered focused when the Y-lambda is sharp, showing high contrast between lines and gaps, otherwise the system is out of focus. The coarse focusing of an HS image can be performed through Y-lambda image inspection. An Y-lambda image from a micrometer contains both low luminance areas (corresponding to the micrometer marks) and the high luminance counterpart (related to the blank areas in the calibration slide). In this work, we used the micrometer scale from the calibration slide as a focusing target (Fig. 4b). Fig. 6a shows an example of a focused Y-lambda image, while Fig. 6b shows an Y-lambda image out of focus.

For precise focus adjustment, it is mandatory to make use of the spatial profile of the Y-lambda image. This spatial profile is a one-dimensional signal where low luminance values correspond to the micrometer marks, and high luminance values correspond to the blank spaces in the calibration slide. In a focused image, this profile looks like a square signal, showing high contrast between lines and gaps. In opposition, if the system is completely out of focus, the spatial profile will looks like a sinusoidal signal. Partially focused images present a shape similar to a square signal, but revealing soft edges. Fig. 7 shows an example of different spatial profiles of a focusing target. In such figure, the focused spectral profile is drawn using a blue line, a near-focused image is represented using a black line and finally an unfocused image is represented using a red line.

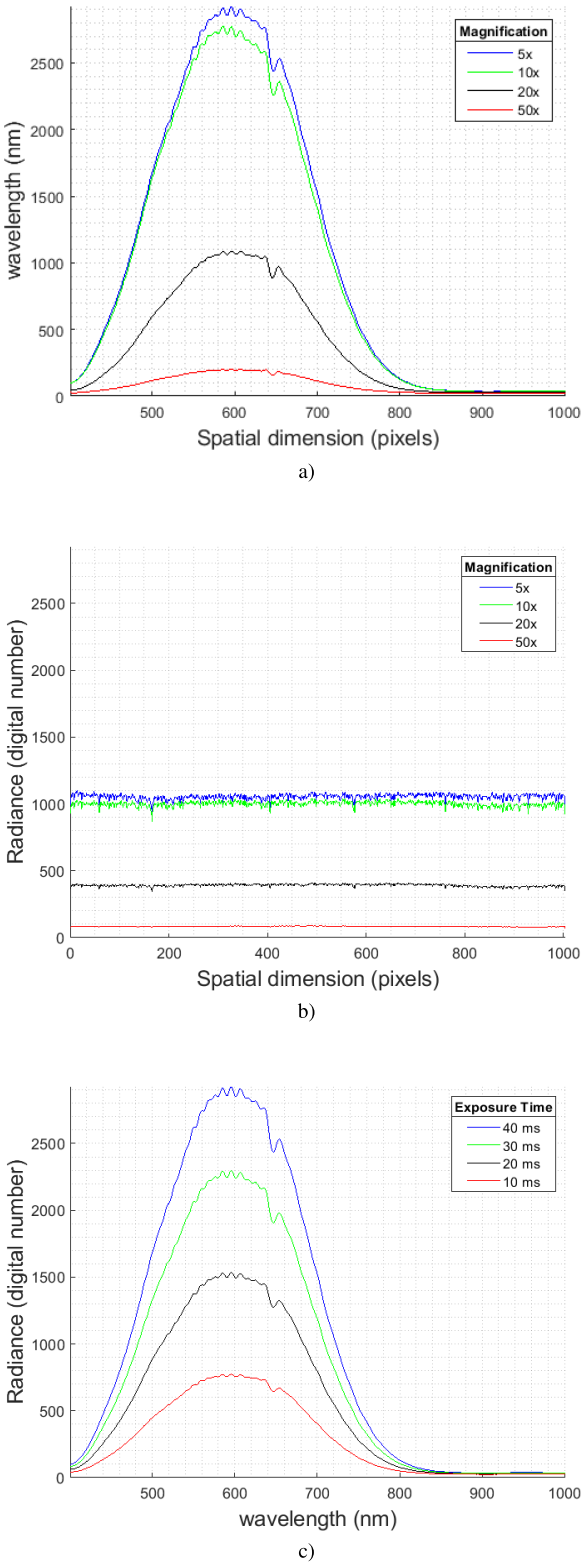

FIGURE 5. Light measurements. a) Spectral and b) spatial distribution of light varying the magnification. c) Spectral distribution of light varying the exposure time.

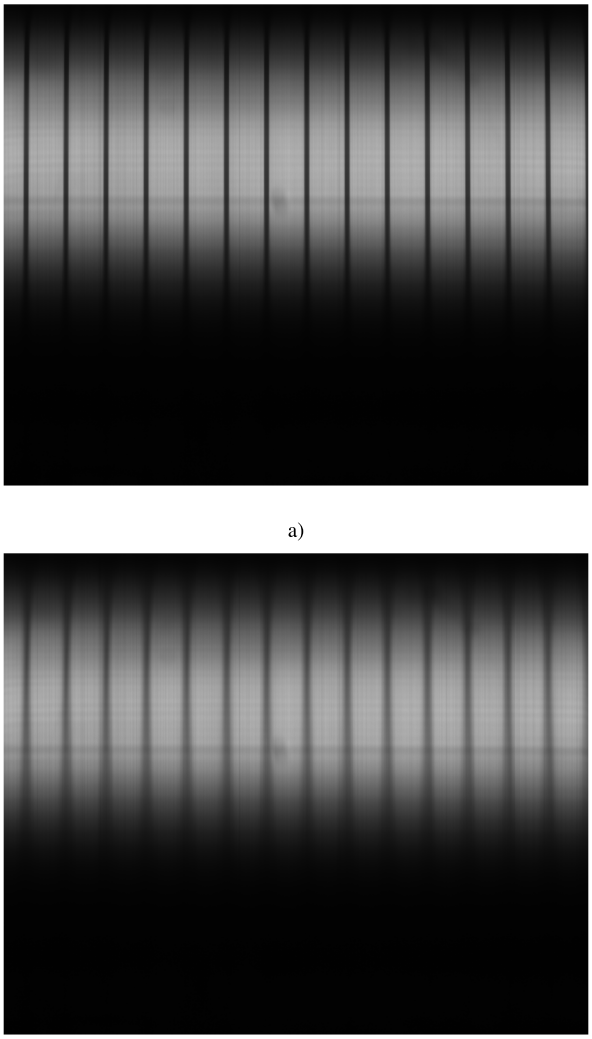

a)

b)

FIGURE 6. Focused (a) and unfocused (b) push-broom frames from a focusing target.

C. MICROSCOPE-HS CAMERA ALIGNMENT

In the following sections, we will extract some information about the precision of our acquisition system by measurements taken from a calibration slide. For some of these measurements, the calibration slide and the FOV of the push-broom camera are required to be correctly aligned. The calibration slide is fixed on the microscope stage, so the only manner to align the camera and the calibration slide is by rotating the camera position relative to the microscope mount. As a coarse alignment methodology, we propose to make use of the micrometer ruler. Fig. 8 shows a representation of two different push-broom frames within a micrometer ruler. The solid line (p_2) represents an scenario where the camera and the microscope stage are aligned, being the FOV of the camera perpendicular to the ruler marks. By contrast, the dashed line (p_1) shows an example of a misaligned setup, where the FOV of the camera is not perpendicular to the sample.

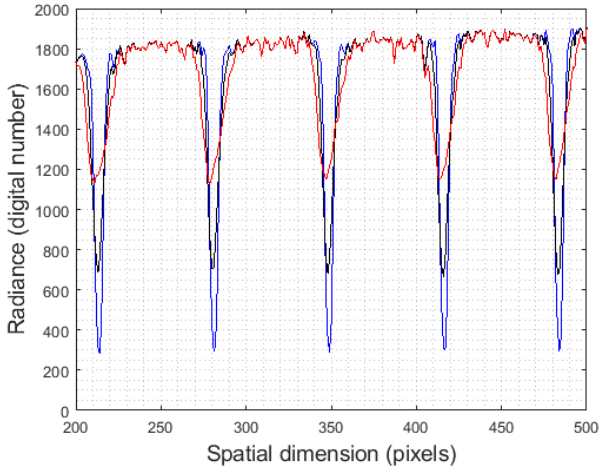

FIGURE 7. Examples of a focused (blue), unfocused (red) and near focused (black) push-broom frames using a spectral profile.

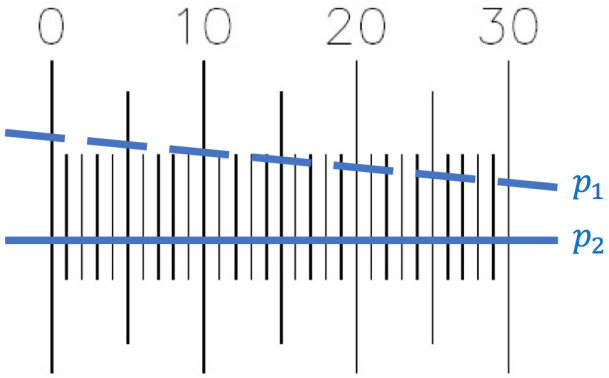

FIGURE 8. Example of the spatial location of different push-broom frames within a micrometer ruler. The blue solid line (p_2) represents a correct alignment, while blue dashed line shows misalignment (p_1).

In this example situation, the camera's FOV was placed exactly at the end of the micrometer marks to facilitate the misalignment detection. In this scenario, when the camera and the microscope stage are properly aligned, the Y-lambda image present a similar shape to Fig. 9a. Furthermore, when the FOV and the sample are aligned, there is no variation in the observed Y-lambda image when manually varying the position of the push-broom frame relative to the sample. Conversely, when FOV position is not perpendicular to the sample (Fig. 8, red dashed line) the Y-lambda image looks like Fig. 9b, where some of the micrometer marks are missing, revealing misalignment.

In order to perform the coarse alignment, we propose to iteratively rotate the HS camera position relative to the microscope stage while visualizing the Y-lambda image. A most reliable methodology to align the HS camera once its coupled to the microscope will be covered later in this manuscript, Section IV-F.

D. SPATIAL RESOLUTION MEASUREMENT

In this section, we aim to determine the effective FOV measured by the HS camera, which also will reveal the width

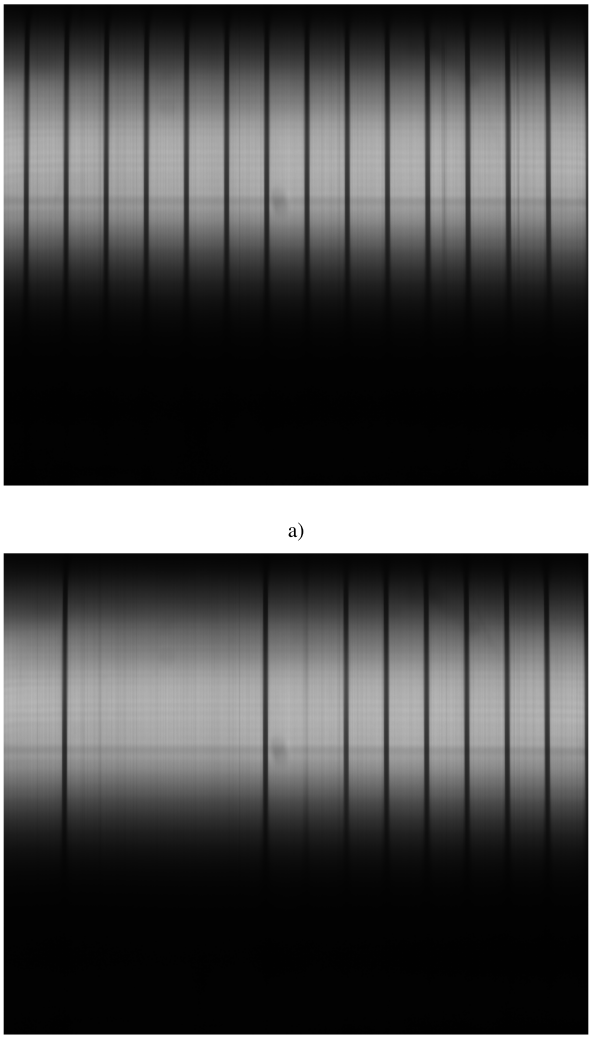

a)

b)

FIGURE 9. Aligned (a) and not aligned (b) frame of the HS camera respect to the sample.

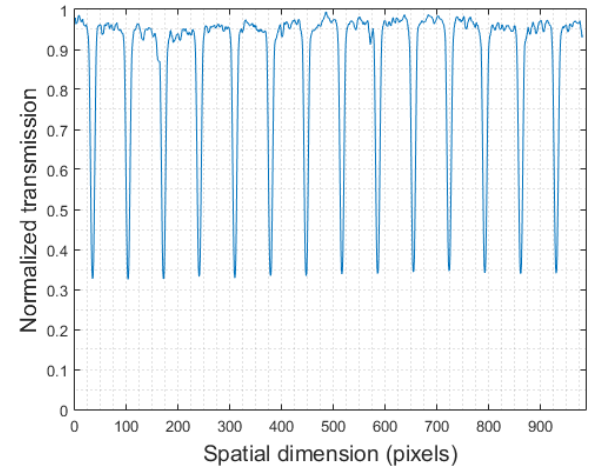

a)

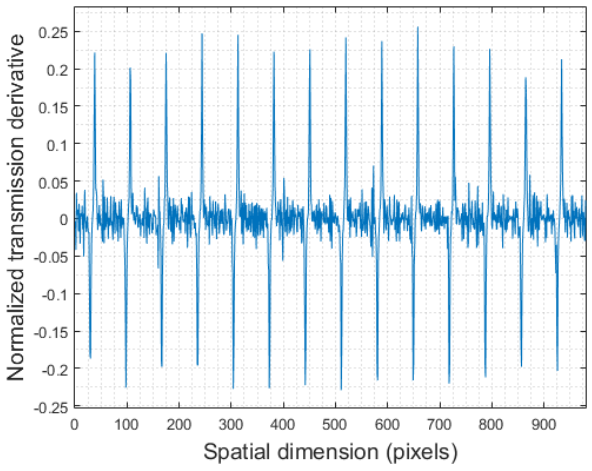

b)

FIGURE 10. Information extracted from the micrometer ruler. a) Ruler spatial profile. b) Ruler profile derivative.

of the push-broom line. This measure allows to determine the proper scanning speed. As mentioned before, the camera should be correctly aligned prior to this step in order to avoid undesired measurement errors. For the FOV measurement, both the micrometer ruler and the dual axis scale (Fig. 4b and Fig. 4c) from the calibration slide are used. Using both calibration targets, it is possible to record images where the distance between lines is known, and hence we can estimate the effective FOV of the camera by performing image analysis over these targets. The setup of this experiment consists on positioning the FOV of the camera within the micrometer scale. For measurements to be correct, the microscope and the HS camera should be correctly aligned, being the situation similar to the one shown in Fig. 8, p_2. The associated Y-lambda image is exactly the same as shown in Fig. 9a.

Our image analysis approach finds to determine the distance (in pixels) between two consequent lines (as drawn in Fig. 8, p_2) by finding the edges of the ruler lines, and counting the pixels between edges in order to estimate the FOV of the HS camera. To this end, we first extract the spatial ruler profile from the Y-lambda image. Then, we search for the edges of the Y-lambda image by calculating the first derivative of the ruler profile. The ruler profile and its derivative are shown in Fig. 10. The positive peaks from Fig. 10b corresponds to the rising edges, and the negative peaks to the falling edges of the ruler profile.

Prior to estimate the distance between lines, we have to find the peaks within the ruler first derivative. To this end, we set a threshold to identify the positive and negative peaks within the ruler derivative profile. Once the peaks are located, we estimate the mean distance (in pixels) between two consecutive peaks of the same sign (positive peaks and negative peaks respectively). The distances are calculated independently for the rising edges and for the falling edges of the ruler profile. In Fig. 11 the peaks corresponding to rising edges are marked in red, while the falling edges counterpart

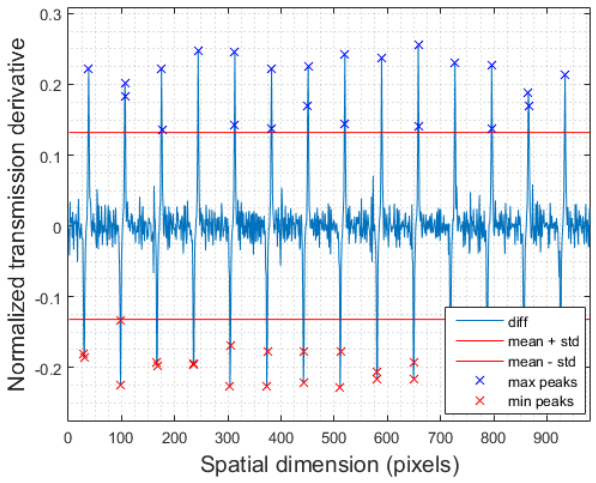

FIGURE 11. Distance calculation based on the ruler's profile derivative.

are marked in blue. Once these peaks are identified, it is possible to calculate the distance between two consecutive lines as the mean of both distances (between positive and negative peaks). Using this distance, we are able to retrieve an estimation about the pixel size, and hence, about the FOV.

In this experiment, the estimation of the FOV was carried out for three different magnifications (5x, 10x and 20x), and the micrometer scale allows to measure three different distances (0.1 mm, 0.05 mm and 0.01 mm). Prior to show the experimental estimation of the FOV for each magnification, some considerations should be highlighted. First, although the calibration slide allows measuring three different distances, the width of the line for 0.05 mm and 0.01 mm divisions keeps constant. For this reason, measures using the 0.01 mm ruler are highly biased by the line width. For an adequate FOV estimation using this methodology, the micrometer ruler should present a low line width compared to the distance between consequent lines.

Although the proposed methodology to measure the FOV is straightforward, the image analysis method will strongly depend on the threshold used to identify the ruler edges within the derivative. Threshold values will be related to the magnification and the distance of the ruler. Assuming that R_d is the first derivative of the ruler profile, we propose to detect the peaks within the ruler's derivative using the threshold defined in (5). Nevertheless, the manual determination of the constant k to be general enough for the different scenarios (varying magnifications and line widths) is difficult. For this reason, to tackle with the manual determination of a threshold, and to fully automate the process, k was determined using a non-linear fitting of manually picked k values for the different magnifications and ruler distances. We found that a third-grade polynomial fit provides enough generalization over our process.

$$threshold = mean(R_d) + k * std(R_d) \tag{5}$$

TABLE 1. Measured FOV (μm).

Distance	5x	10x	20x
0.1	1470.62	733.94	366.30
0.05	1492.58	738.01	368.32
0.01	1538.53	800.00	392.16
Theoretical	1500	750.46	375.23

Using this methodology, we found agreement between the estimated FOV using (1) and the measured FOV using the ruler profile, as we can see from results collected in Table 1.

E. EMPIRICAL ASSESSMENT OF THE MECHANICAL MOVEMENT PRECISION AND REPEATABILITY

As described in Section III-B, the mechanical resolution of the system is a critical characteristic for being able to acquire high-quality images. Due to this reason, a stepper motor has been set up in the microscope using a custom 3D printed mechanism for automatically controlling the sample movement and theoretically achieving a very high movement resolution ($D_{linear} = 0.1640625$ micrometers). In on order to verify the precision of the developed mechanism as well as its repeatability and tolerance, the linear displacement of the microscope stage in the X direction when rotating the motor 200,000 steps has been measured using a digital caliper gauge. For doing so, the digital caliper gauge has been installed also using custom design 3D printed parts. Using this set up, a set of 10 measurements have been taken. The average obtained distance was 32.941 mm with a standard deviation lower than the 0.3%. According to this value, the minimal distance that the sample could be moved (mechanical resolution) is 0.164705 μm. As it can be observed, this value is very closed to the theoretically calculated one ($D_{linear} = 0.1640625\mu$m), being the difference lower than 0.5%.

F. SYSTEM SPEED AND ALIGNMENT CALIBRATION IMPROVEMENT

At this stage of the calibration process, the camera has been aligned by visual inspection, as described in Section IV-C. The pixel size has also been calculated using the methodology described in Section III-A. Additionally, the spatial resolution of the system is also known (calculated in Section III-B). Using the pixel size, the mechanical resolution and the capturing frame rate of the HS camera, the required motor rotation speed can be calculated using (3), as it was described in Section III-B. Hence, relatively good HS images should be obtained using this set up. Nevertheless, one extra stage is carry out in this section in order to slightly improve and/or verify the correct execution of the previous calibration stages. In this calibration stage the entire acquisition system (microscope, camera and movement mechanism) is considered as a whole. The goal is to take a picture of a circle of the calibration slide and evaluate its spatial appearance in order to determine possible camera misalignment's and/or not optimal

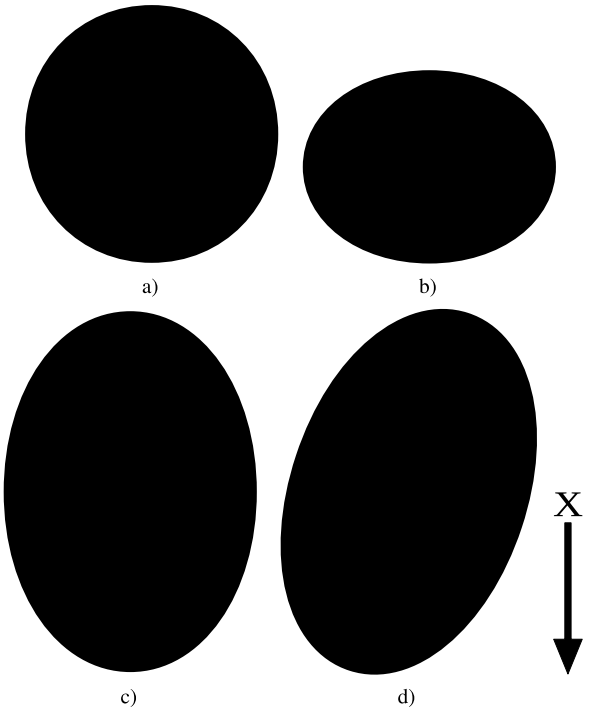

FIGURE 12. Possible scenarios when capturing a circle (Movement in the X direction). a) Correct motor speed. b) Motor speed is too high, camera is aligned. c) Motor speed is too low, camera is aligned. d) Motor speed is too low, camera is misaligned.

movement speeds. Fig. 12 graphically indicates the different scenarios that may be faced in this process.

As it can be seen in Fig. 12, when the image of the circle of the calibration slide is taken at the correct speed, it shapes perfectly corresponds with a circle (Fig. 12a). However, when the speed is too high or too low, its shape seems like an ellipse (Fig. 12b and 12c, respectively). Additionally, when the camera is not correctly aligned, the circle seems to be slightly rotated. However, this effect can be better perceived when the speed is too low and the circle seems outstretched (Fig. 12d). Accordingly, in order to verify the correct alignment of the camera, a low speed can be forced in this experiment.

Despite a relatively good assessment of the correct system calibration can be done by visual inspection, an automatic methodology has been used in order to make it in a more precise and rigorous manner. For such purpose, the circle (or ellipse) eccentricity has been used together with a principal component analysis (PCA) method. The employed automatic methodology is described as follows:

- *Image binarization.* The image is firstly binarized generating a single 2D classification map where the pixels corresponding to the circle are labeled as 1 and the background pixels are labeled as 0. This is a relatively straight forward process considering that once that the image is calibrated, the HS pixels corresponding to the circle already have very low values and the background pixels have very high ones.
- *Principal components extraction.* A 2D principal component analysis is computed over the binarized classification map. This analysis provides two eigenvalues, corresponding to the directions of the longest and shortest axes of the ellipse (λ_{max} and λ_{min}), as well as their corresponding eigenvectors, which conform the rotation matrix, as shown in Fig. 13.

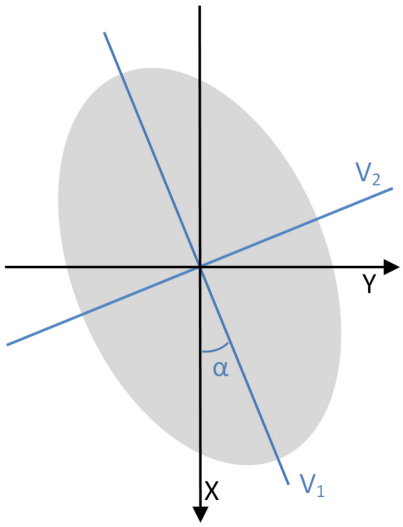

FIGURE 13. Principal component analysis of the pixels that conform the ellipse. X represents the sample moving direction. V_1 and V_2 represent the eigenvectors corresponding to the λ_{max} and λ_{min} eigenvalues, respectively. α represents the rotation angle.

- *Eccentricity calculation.* The eccentricity of the ellipse can be expressed in terms of its major and minor (ϕ_{max} and ϕ_{min}) axes as shown in (6). In order to simplify the calculations, we are using the two eigenvalues extracted in the previous stage in order to calculate the eccentricity, as shown in (6), taking advantage of the fact that $(\phi_{min})^2/(\phi_{max})^2 = \lambda_{min}/\lambda_{max}$. Using this methodology, when the speed at which the sample is moved is perfectly fixed according to the pixel size and the camera frame rate, the obtained eccentricity (e) should be ideally 0.

$$e = \sqrt{1 - \frac{(\phi_{min})^2}{(\phi_{max})^2}} = \sqrt{1 - \frac{\lambda_{min}}{\lambda_{max}}} \tag{6}$$

- *Rotation angle calculation.* Using the first eigenvector of the rotation matrix, V_1, which corresponds to the first eigenvalue, the "counterclockwise" rotation angle, with respect to the X axis, α, can be calculated as shown in (7). For simplicity, we are always considering the first eigenvalue as the largest one, and hence, the rotation angle can be represented as shown in Fig. 13. This angle is equivalent to the camera misalignment. If the obtained angle value is 0° or 90°, it means that the camera is perfectly aligned. Notice that for making this calculation is better to set a relatively low speed in order to obtain an outstretched appearance of the ellipse, being 0° the desirable angle value. If a relatively high speed were used, the desirable angle value would be 90°. It is also important to highlight that the axis are rotated 90° clockwise so that the X axis of the capture image corresponds

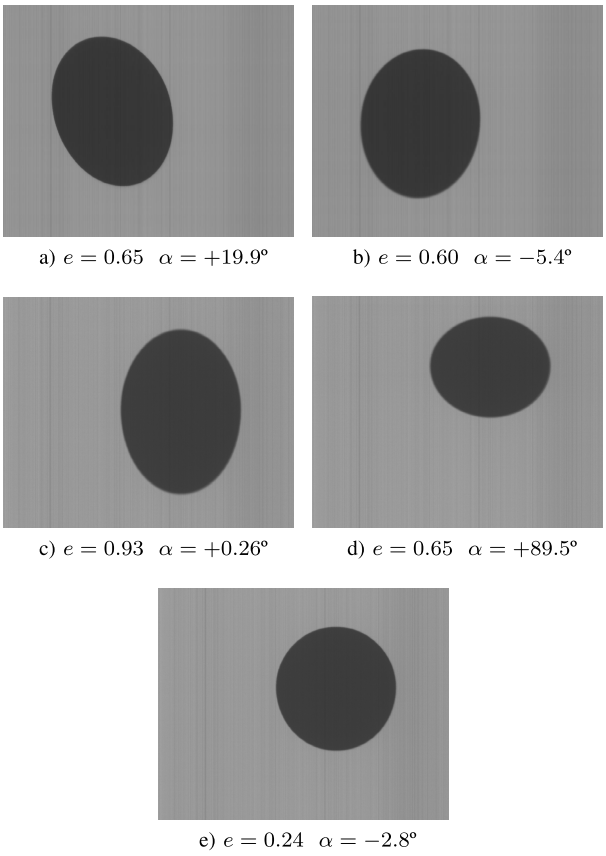

FIGURE 14. Real examples of the results provided by the described methodology. a-b) Examples of misaligned HS images. c-d) Examples of images acquired with a bad scanning speed configuration. e) Image acquired with correct alignment and speed conditions.

with the sample moving direction (X).

$$\alpha = \arctan(\frac{V_{1_y}}{V_{1_x}}) \tag{7}$$

Fig. 14 displays a set of example HS images collected by the described system, as well as the alignment and eccentricity values provided by the described method. On the one hand, Fig. 14a and 14b display a set of images collected with the HS camera misaligned and at a relatively low speed in relation to the optimal capturing speed for the specified frame period and pixel size. The low speed was established in order to highlight the misalignment in the dot circle sample, which cannot be appreciated in optimal scanning speed conditions. Such images are useful for obtaining the rotation angle that needs to be applied to the HS camera in each situation in order to correctly align it. On the other hand, Fig. 14c and 14d display a set of images collected with the camera already aligned but using different speeds. In these images we can observe that the measured rotation angle is close to either 0 or 90 degrees, while the rotation angle calculated from Fig. 14a and 14b indicate a misalignment between the camera and the microscope. Nevertheless, the eccentricity values calculated for Fig. 14c and 14d is not close to zero, which indicates that the circle dots were not captured using an appropriate scanning speed. Finally, Fig. 14e show a HS cube captured in adequate conditions, i.e. the scanning speed is correctly configured and the microscope and the HS camera are aligned. In such example, the value of the eccentricity is close to zero, indicating that the image was acquired in adequate conditions.

G. CALIBRATION

The goal of HS acquisition systems is to provide a spectral signature per spatial pixel of the captured scene. These spectral signatures indicate the percentage of incident radiation at each spatial pixel that the scanned object transmits or reflects at each captured wavelength.

As already mentioned in Section II, the spectral response of an HS acquisition system is affected by several factors, namely the intrinsic spectral response of sensor, the light transmission through the lenses and optical elements, and the spectral shape of the light source. Due to this reason, in order to obtain spectral signatures that really indicate the percentage of transmitted or reflected radiation at each of the different wavelengths, the data acquired by the HS system need to be radiometrically calibrated. This calibration consists in normalizing the captured HS pixels by linearly scaling their values considering the maximum and minimum values that the sensor could measure if the scanned object transmitted the 100% and 0% of the incident radiation. This calibration must be done in the exact same capturing conditions that the HS image is taken.

The next process is followed in order to carry out this calibration process. First of all, once the adequate capturing conditions (exposure time, light intensity, etc.) have been set up, the sample slide is positioned at a blank area. Then, an HS frame is obtained at this position. This HS frame is typically referred as *White Reference*, (WR). Since there is not any sample material in such position of the slide, this HS frame contains the maximum values that the sensor is able to measure for each pixel and band in the specified capturing conditions (exposure time, light intensity, etc.). Afterwards, the light source is turned off and a new HS frame is collected. This HS frame is typically referred as *Dark Reference*, (DR), and contains the minimum values that system is able to provide for each pixel and band. Ideally, the DR values should be very close to zero, however higher values may be obtained, typically due to the intrinsic noise of the sensor. Once the WR and DR have been collected, the light source is turn on again and the HS image is captured. Each HS frame of the captured image is radiometrically calibrated using the WR and DR as shown in (8), where Raw_i refers to the i^{th} HS frame of the acquired image while r_i refers to the same frame after the radiometric calibration. Additionally, in order to mitigate the noise influence, the WR and DR are collected 100 times each, thus calculating their average values.

$$r_i = \frac{Raw_i - DR}{WR - DR} \tag{8}$$

Fig. 15 shows an example of how the spectral signatures of different pixels are scaled to transmittance values using the

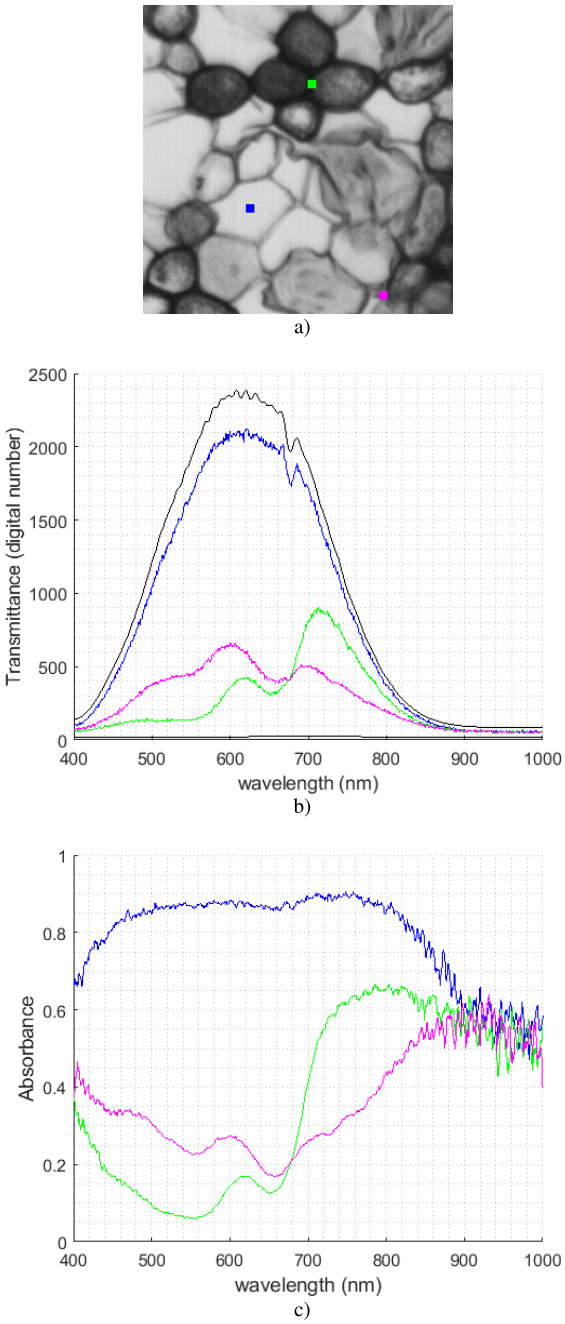

FIGURE 15. Example of the effect of calibration in the spectral signatures. a) Selected pixel within an example image. b) Uncalibrated spectral signatures. c) Calibrated spectral signatures.

aforementioned radiometric calibration process. This effect is shown for certain pixels within an example image (Fig. 15a). Concretely, Fig. 15b shows the uncalibrated raw spectral signatures, including the spectral signatures of the white and dark references (WR and DR), representing with the black color lines. Fig. 15c shows the same spectral signatures after applying the calibration procedure. The effect of scaling the spectral values to reflectance or transmitance values can also be observed in Fig. 16a and 16b where RGB images are obtained using the spectral bands centered at 709.0, 539.5 and 479.6 nm, respectively.

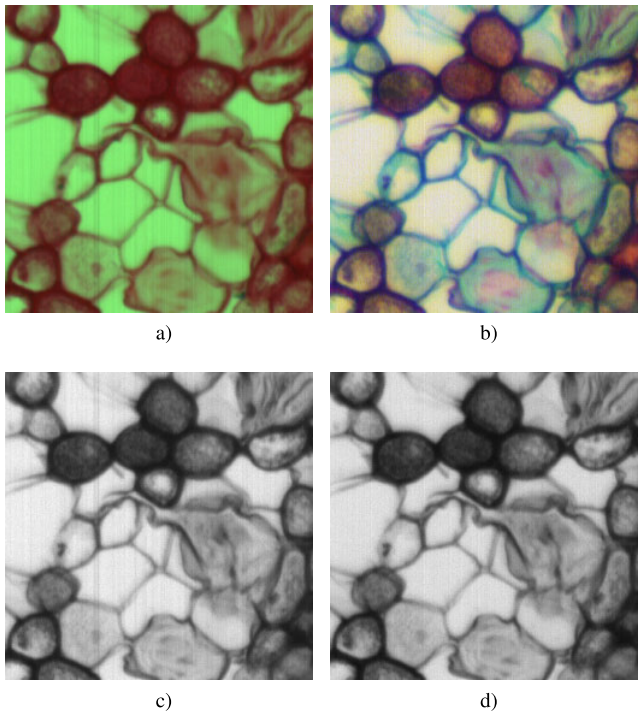

FIGURE 16. Real examples of the uncalibrated and calibrated spectral images. a) Uncalibrated RGB image (709.0, 539.5 and 479.6 nm). b) Calibrated RGB image (709.0, 539.5 and 479.6 nm). c) Uncalibrated single image band (539.5 nm). d) Calibrated single band image (539.5 nm).

Additionally, the calibration process also helps to remove the stripping noise effect, which typically appears when acquiring HS images using push-broom scanners [29]. The stripping noise consists in spatially coherent lines that appear in the spatial scanning axis due to static artifacts produced in the sensors, that are repeated in each push-broom frame, as shown in Fig. 16a and 16b. In the calibrated images, the effect of the stripping noise disappear (Fig. 16b and 16d).The stripping noise is mainly due to the fact that different photo-receptors of the sensor have slightly different sensibility, producing slightly different values when measuring the exact same amount of incident radiation.

H. COMMON DEFECTS IN HS IMAGES

In this section, we show some examples of how the images look like when the set up of the HS acquisition system is not appropriate. To this end, we collected images from the micrometer ruler grid (Fig. 4c). Images were collected using the 20x magnification for this experiment. To perform the comparative between the different scenarios, we show the panchromatic images from the original HS cubes, i.e. we average all spectral channels and visualize the defects spatially. Fig. 17a shows an HS image collected in adequate conditions.

In Fig. 17b, we can observe an unfocused image. The image is not sharp, and hence small details are lost. Although it is desirable a proper focusing, there are several techniques to enhance the quality of badly focused images [30]. Besides, we can see the effect of an image captured when the camera

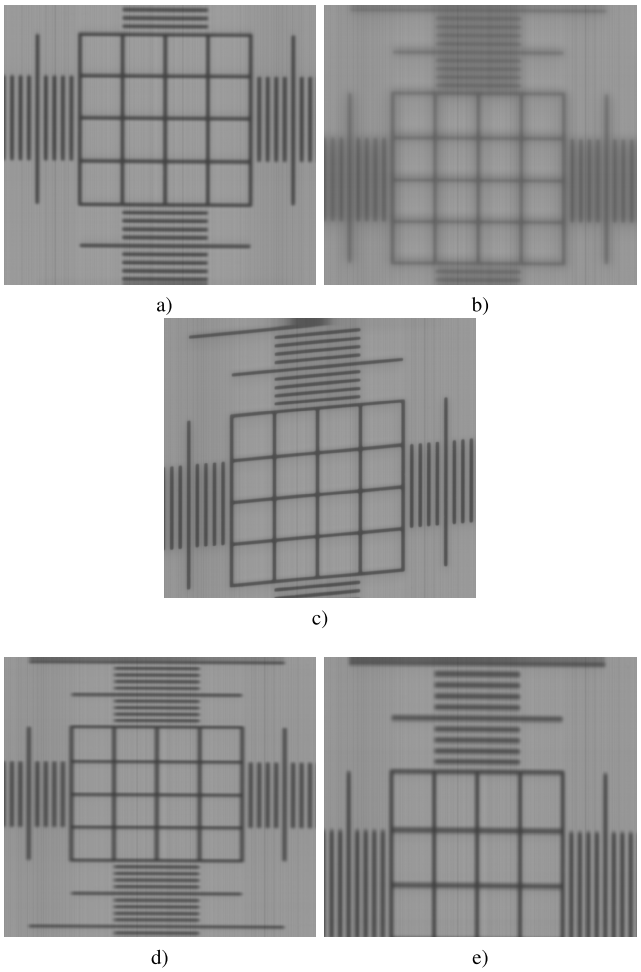

FIGURE 17. Common defects in HS images. a) Correct HS image b) Unfocused image. c) Misaligned image. c-e) Bad speed configuration (fast and low scanning speed respectively).

and the microscope stage are not correctly aligned in Fig. 17c. As far as the spectral information is concerned, there will be not change in the spectral signature of different materials in a misaligned image. Nevertheless, this misalignment can cause morphological deformations over the sample, which has to be avoided in applications where the morphological features of the samples are important.

Finally, we show the effect of a bad scanning speed configuration. On the one hand, if the scanning speed is fast compared to the sensor frame rate, some lines of the scene will be skipped, resulting in the loss of some information from the scene. The spatial appearance of a fast scanning speed can be visualize in Fig. 17d, where the shape of the image seems to be flat compared with the original one. On the other hand, if the scanning speed is slow compared to the acquisition time, each line of the spatial scanning is re-sampled, resulting in a outstretched image of the original sample, Fig. 17e.

V. CAPTURING REAL SAMPLES

Finally, Fig. 18 shows different representations of HS data collected from real samples using the described

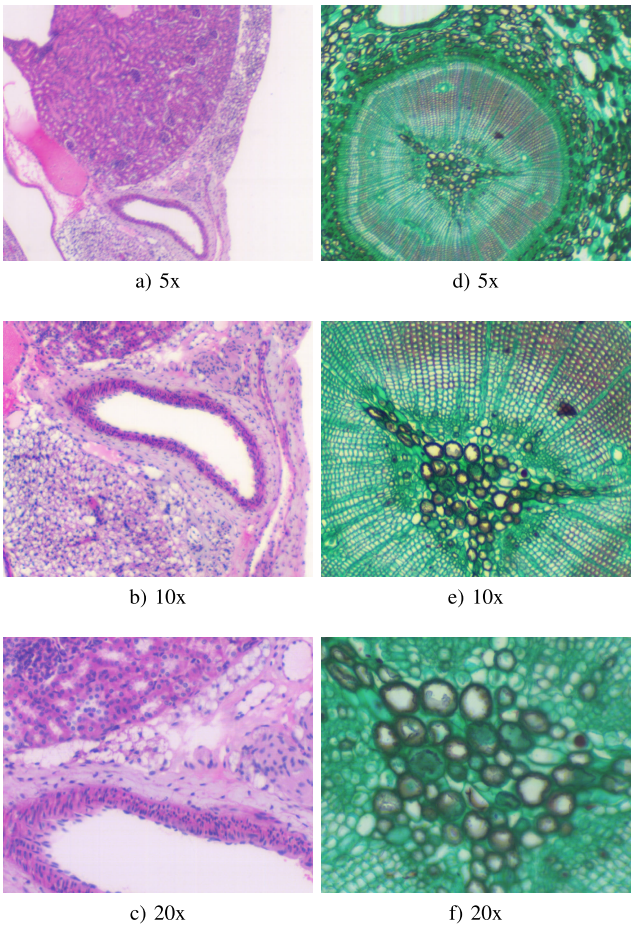

FIGURE 18. RGB representation of the HS data collected using different magnifications for the rat kidney histology sample (a-c) and for the pine stem sample (d-f).

acquisition system at different magnifications. The specimens under evaluation are prepared slides from Brunel Microscopes (Brunel Microscopes, Wiltshire, U.K.), Specifically, we imaged a pine stem sample (BS17 Stem Structure) and a rat kidney histology sample (BS28 Rat Histology).

Fig. 18a-f display a RGB representation of the data acquired using 5x, 10x and 20x magnifications from the BS28 Rat Histology and BS17 Stem Structure samples, respectively. As it happens in any microscope system, more spatial details can be observed for higher magnifications. Besides, Fig. 19 shows some spectral signatures extracted from the HS data acquired using the 20x magnification. Each of these spectral signatures corresponds to one HS pixel of the image. As it can be observed, there are many differences in the spectral signatures displayed for both data sets. This suggests the presence of different materials and provides the possibility of distinguishing them using their spectral characteristics, what justifies using microscope acquisition systems based on HS push-broom scanners for many different applications, such as [12], [24], [31]–[34]. It can also be observed that the pixel size increases for lower magnifications, and targets that can be clearly distinguished using higher magnifications appear mixed in a single pixel. This results in

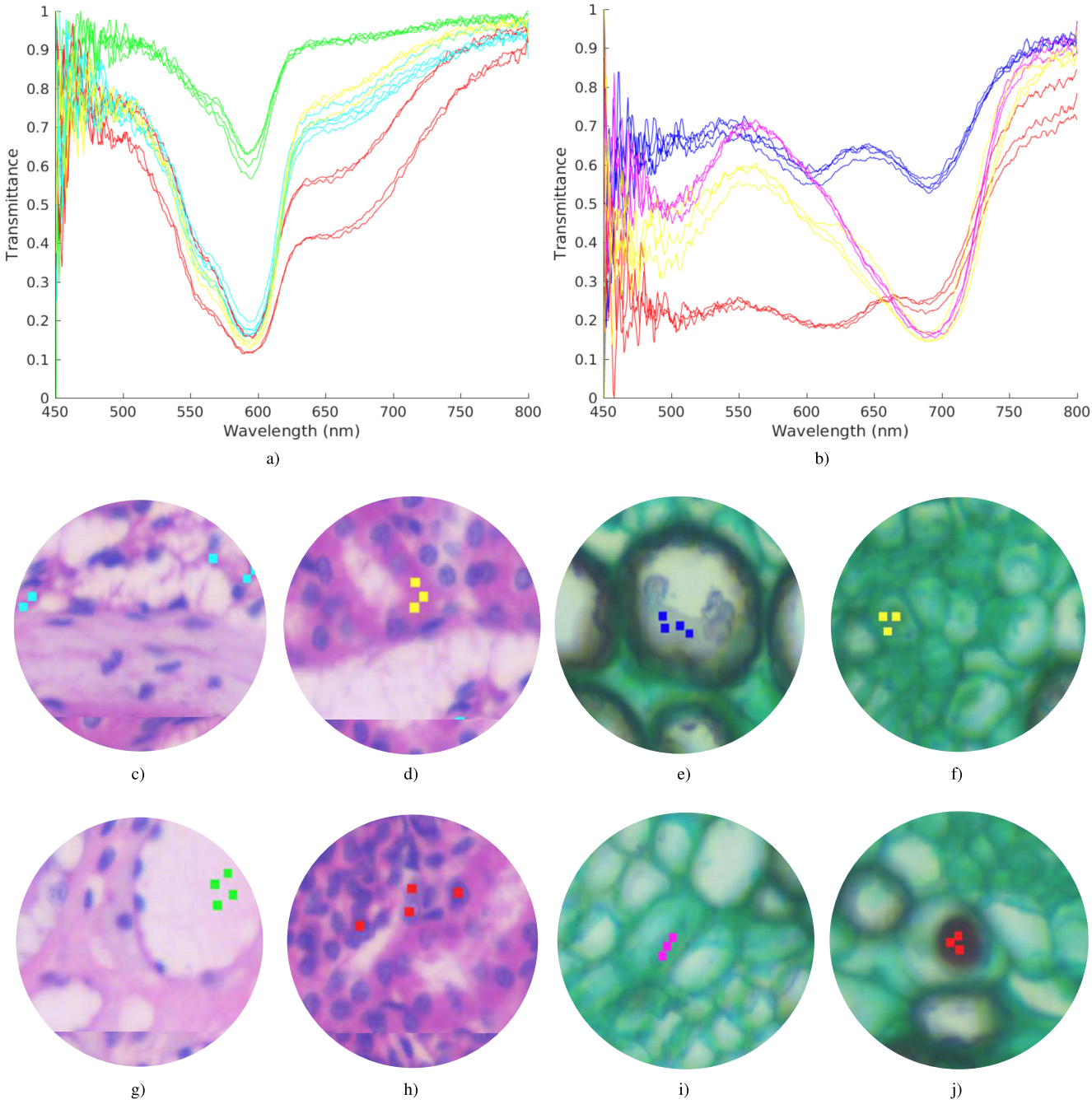

FIGURE 19. Spectral signatures present in the rat kidney histology sample (a) and the pine stem sample (b). Pixels corresponding to the rat histology sample are shown in subfigures (c), (d), (g) and (h). Pixels corresponding to the pin stem sample are displayed in subfigures (e), (f), (i) and (j).

mixed spectral signatures [35] making more challenging the detection of some specific targets, what justifies the use of high magnifications and resolutions for some applications where the targets to be analyzed are especially small.

VI. CONCLUSION

Currently, most researchers are evaluating if the HS analysis of different types of microscopic samples can provide some benefits compared to the traditional analysis of such samples in different fields. For this reason, in most situations neither the optimal spectral range nor the spectral resolution to be used in a given application are known beforehand. Among other HS technologies, push-broom cameras present high spectral resolution, and are the ones able to capture HS images in the NIR or SWIR spectral ranges, making them a very interesting technology in this field.

In this manuscript, we present a methodology to correctly set-up a push-broom HS microscope to acquire high-quality HS images. The main motivation of this manuscript is to propose a sorted list of automatic and semi-automatic tasks that

should be executed prior to acquire high-quality microscopic HS images using push-broom cameras. This methodology has been tested using a Hyperspec©VNIR A-Series from HeadWall Photonics coupled to an Olympus BH2-MJLT microscope, using a self-developed 3D printed mechanism for accomplishing the required mechanical movements, which provides a low-cost alternative to commercial motorized microscope stages. Nevertheless, the proposed methodology is intended to be general enough to be suitable for whatever microscope and whatever push-broom HS camera is used. This methodology involves the set up of the light conditions, the optical focusing of the system, the camera alignment and the set up of the optimal scanning speed. In addition, it allows the empirical measurement of both the FOV and the mechanical resolution of the scanning platform, as well as detecting and characterizing the limitations of the acquisition system under analysis.

Concretely, a method for characterizing the HSI dynamic ranges and the latter optimization of the intensity of the light source and exposure time of the camera to achieve optimal illumination conditions is firstly proposed. Secondly, a method for correctly focusing the HS camera is introduced using calibration slides and Y-lambda images. Thirdly, a method for calculating the adequate scanning speed is introduced, which requires the previous knowledge of the pixel size and the mechanical resolution of the scanning platform. In case that these values are not known in advance, a methodology for empirically calculating them is also described. Finally, a semi-automatic method based on PCA is introduced, which helps the user to precisely carry out the HS camera alignment as well as fine tuning the scanning speed. Additionally, this method for fine-tuning the scanning speed of a push-broom camera can be directly used even if the technical details of neither the optical system nor the mechanical system are known. However, the set up process may take considerably less time if an initial speed value closed to the optimal one is set.

The methodology presented in this manuscript is intended to provide a fast and accurate configuration of HS push-broom microscopes for researchers in this field. To be able to apply this methodology, a HS push-broom camera and a mechanism able to perform the linear movement of the sample are needed. Any push-broom camera is suitable to be used in the application of the proposed methodology, i.e. to perform the experiments regarding the dynamic range and the FOV measurements. As far as the mechanism is concerned, although in this manuscript we employed a custom 3D printed mechanism, commercial mechanisms are also compatible with our methodology. To perform the steps of this methodology which involve a linear movement mechanism, the only requirement is to be able to control by software both the speed and the movement of the movement mechanism.

Although in this manuscript we present some quantitative outcomes (such as the relationship between the theoretical values of the FOV or the mechanical resolution and the experimental ones), we have not performed a quantitative measurements of the overall quality of the acquired HS images, both spatially and spectrally. In future works, we are planning to further investigate in this field in order to provide measurements of the quality of the HS images obtained by the acquisition system.

After applying this methodology to our own acquisition system, some of its limitations have been found out. Particularly, it has been observed that the illumination conditions are not optimal. The dynamic range cannot be maximized due to limitations in the light source power and also in the exposure time (which has an upper limit of 40 *ms*). To improve the dynamic range conditions in this scenario, an external light source could be used. Additionally, in the acquisition system under analysis, the focus is carried out manually by the user. Although we are able to acquire good quality images when focusing manually, a better focus plane configuration could be achieved if the Z-axis of the microscope were motorised.

REFERENCES

[1] M. Govender, K. Chetty, and H. Bulcock, "A review of hyperspectral remote sensing and its application in vegetation and water resource studies," *Water SA*, vol. 33, no. 2, pp. 1–8, 2007.

[2] G. M. ElMasry and S. Nakauchi, "Image analysis operations applied to hyperspectral images for non-invasive sensing of food quality—A comprehensive review," *Biosyst. Eng.*, vol. 142, pp. 53–82, Feb. 2016.

[3] F. D. van der Meer, H. M. A. van der Werff, F. J. A. van Ruitenbeek, C. A. Hecker, W. H. Bakker, M. F. Noomen, M. van der Meijde, E. J. M. Carranza, J. B. de Smeth, and T. Woldai, "Multi-and hyperspectral geologic remote sensing: A review," *Int. J. Appl. Earth Observ. Geoinf.*, vol. 14, no. 1, pp. 112–128, 2012.

[4] D. G. Ferris, R. A. Lawhead, E. D. Dickman, N. Holtzapple, J. A. Miller, S. Grogan, S. Bambot, A. Agrawal, and M. L. Faupel, "Multimodal hyperspectral imaging for the noninvasive diagnosis of cervical neoplasia," *J. Lower Genital Tract Disease*, vol. 5, no. 2, pp. 65–72, 2001.

[5] H. Akbari, L. Halig, D. M. Schuster, B. Fei, A. Osunkoya, V. Master, P. Nieh, and G. Chen, "Hyperspectral imaging and quantitative analysis for prostate cancer detection," *Proc. SPIE*, vol. 17, no. 7, 2012, Art. no. 076005.

[6] A. O. N. Joseph, *Hyperspectral Optical Imaging for Detection, Diagnosis and Staging of Cancer*. Los Angeles, CA, USA: Univ. of Southern California, 2012.

[7] H. Fabelo, M. Halicek, S. Ortega, M. Shahedi, A. Szolna, J. Piñeiro, C. Sosa, A. J. O'Shanahan, S. Bisshopp, C. Espino, M. Márquez, M. Hernández, D. Carrera, J. Morera, G. M. Callico, R. Sarmiento, and B. Fei, "Deep learning-based framework for *in vivo* identification of glioblastoma tumor using hyperspectral images of human brain," *Sensors*, vol. 19, no. 4, p. 920, Feb. 2019.

[8] M. Halicek, H. Fabelo, S. Ortega, G. M. Callico, and B. Fei, "*In-vivo* and *ex-vivo* tissue analysis through hyperspectral imaging techniques: Revealing the invisible features of cancer," *Cancers*, vol. 11, no. 6, p. 756, May 2019. [Online]. Available: https://www.mdpi.com/2072-6694/11/6/756

[9] A. F. H. Goetz, "Three decades of hyperspectral remote sensing of the earth: A personal view," *Remote Sens. Environ.*, vol. 113, pp. S5–S16, Sep. 2009. [Online]. Available: https://linkinghub.elsevier.com/retrieve/pii/S003442570900073X

[10] J. A. Richards, *Remote Sensing Digital Image Analysis*. Berlin, Germany: Springer, 2013. [Online]. Available: http://link.springer.com/10.1007/978-3-642-30062-2

[11] R. A. Schultz, T. Nielsen, J. R. Zavaleta, R. Ruch, R. Wyatt, and H. R. Garner, "Hyperspectral imaging: A novel approach for microscopic analysis," *Cytometry*, vol. 43, no. 4, pp. 239–247, 2001.

[12] E. Pirard, "Multispectral imaging of ore minerals in optical microscopy," *Mineralog. Mag.*, vol. 68, no. 2, pp. 323–333, Apr. 2004.

[13] J. van der Weerd, M. K. van Veen, R. M. A. Heeren, and J. J. Boon, "Identification of pigments in paint cross sections by reflection visible light imaging microspectroscopy," *Anal. Chem.*, vol. 75, no. 4, pp. 716–722, 2003.
[14] A.-K. Mahlein, "Plant disease detection by imaging sensors—Parallels and specific demands for precision agriculture and plant phenotyping," *Plant Disease*, vol. 100, no. 2, pp. 241–251, Feb. 2016. [Online]. Available: http://apsjournals.apsnet.org/doi/10.1094/PDIS-03-15-0340-FE
[15] M. Leucker, A.-K. Mahlein, U. Steiner, and E.-C. Oerke, "Improvement of lesion phenotyping in *cercospora beticola*–sugar beet interaction by hyperspectral imaging," *Phytopathology*, vol. 106, no. 2, pp. 177–184, Feb. 2016. [Online]. Available: http://apsjournals.apsnet.org/doi/10.1094/PHYTO-04-15-0100-R
[16] G. Lu and B. Fei, "Medical hyperspectral imaging: A review," *Proc. SPIE*, vol. 19, no. 1, 2014, Art. no. 010901.
[17] B. S. Sorg, B. J. Moeller, O. Donovan, Y. Cao, and M. W. Dewhirst, "Hyperspectral imaging of hemoglobin saturation in tumor microvasculature and tumor hypoxia development," *Proc. SPIE*, vol. 10, no. 4, 2005, Art. no. 044004.
[18] A. M. Siddiqi, H. Li, F. Faruque, W. Williams, K. Lai, M. Hughson, S. Bigler, J. Beach, and W. Johnson, "Use of hyperspectral imaging to distinguish normal, precancerous, and cancerous cells," *Cancer Cytopathol., Interdiscipl. Int. J. Amer. Cancer Soc.*, vol. 114, no. 1, pp. 13–21, 2008.
[19] M. Maggioni, G. L. Davis, F. J. Warner, F. B. Geshwind, A. C. Coppi, R. A. DeVerse, and R. R. Coifman, "Hyperspectral microscopic analysis of normal, benign and carcinoma microarray tissue sections," *Proc. SPIE*, vol. 6091, Feb. 2006, Art. no. 60910I.
[20] Q. Li, X. Yongqi, G. Xiao, and J. Zhang, "New microscopic pushbroom hyperspectral imaging system for application in diabetic retinopathy research," *Proc. SPIE*, vol. 12, no. 6, 2007, Art. no. 064011.
[21] M. L. Huebschman, R. A. Schultz, and H. R. Garner, "Characteristics and capabilities of the hyperspectral imaging microscope," *IEEE Eng. Med. Biol. Mag.*, vol. 21, no. 4, pp. 104–117, Jul./Aug. 2002.
[22] L. Gao and R. T. Smith, "Optical hyperspectral imaging in microscopy and spectroscopy—A review of data acquisition," *J. Biophoton.*, vol. 8, no. 6, pp. 441–456, 2015.
[23] L. Qing-Li, X. Gong-Hai, X. Yong-Qi, and Z. Jing-Fa, "Microscopic hyperspectral image study of human blood cells," *Opto-Electron. Eng.*, vol. 5, pp. 98–101, May 2008.
[24] S. Ortega, H. Fabelo, R. Camacho, M. de la Luz Plaza, G. M. Callicó, and R. Sarmiento, "Detecting brain tumor in pathological slides using hyperspectral imaging," *Biomed. Opt. Express*, vol. 9, no. 2, pp. 818–831, Feb. 2018. [Online]. Available: https://www.osapublishing.org/abstract.cfm?URI=boe-9-2-818
[25] D. G. Manolakis, R. B. Lockwood, and T. W. Cooley, *Hyperspectral Imaging Remote Sensing: Physics, Sensors, and Algorithms*. Cambridge, U.K.: Cambridge Univ. Press, 2016.
[26] L. Jiang, G. Cui, and T. Xu, "Effect of lens on spectral characteristics of imaging system," in *Advances in Graphic Communication, Printing and Packaging*. Singapore: Springer, 2019, pp. 170–177. [Online]. Available: http://link.springer.com/10.1007/978-981-13-3663-8_25
[27] R. W. G. Hunt and M. R. Pointer, *Measuring Colour*. Chichester, U.K.: Wiley, 2011. doi: 10.1002/9781119975595.
[28] N. Kularatna, *Digital and Analogue Instrumentation: Testing and Measurement*. London, U.K.: Institution of Engineering and Technology, 2003. [Online]. Available: https://digital-library.theiet.org/content/books/cs/pbel011e
[29] L. Gómez-Chova, L. Alonso, L. Guanter, G. Camps-Valls, J. Calpe, and J. Moreno, "Correction of systematic spatial noise in push-broom hyperspectral sensors: Application to CHRIS/PROBA images.," *Appl. Opt.*, vol. 47, no. 28, pp. F46–F60, Oct. 2008. [Online]. Available: http://www.ncbi.nlm.nih.gov/pubmed/18830284
[30] X.-L. Zhao, F. Wang, T.-Z. Huang, M. K. Ng, and R. J. Plemmons, "Deblurring and sparse unmixing for hyperspectral images," *IEEE Trans. Geosci. Remote Sens.*, vol. 51, no. 7, pp. 4045–4058, Jul. 2013.
[31] Y. Khouj, J. Dawson, J. Coad, and L. Vona-Davis, "Hyperspectral imaging and K-means classification for histologic evaluation of ductal carcinoma *in situ*," *Frontiers Oncol.*, vol. 8, p. 17, Feb. 2018. [Online]. Available: http://journal.frontiersin.org/article/10.3389/fonc.2018.00017/full
[32] Y. Duan, J. Wang, M. Hu, M. Zhou, Q. Li, L. Sun, S. Qiu, and Y. Wang, "Leukocyte classification based on spatial and spectral features of microscopic hyperspectral images," *Opt. Laser Technol.*, vol. 112, pp. 530–538, Apr. 2019. [Online]. Available: https://linkinghub.elsevier.com/retrieve/pii/S0030399218309800
[33] Q. Wang, L. Chang, M. Zhou, Q. Li, H. Liu, and F. Guo, "A spectral and morphologic method for white blood cell classification," *Opt. Laser Technol.*, vol. 84, pp. 144–148, Oct. 2016. [Online]. Available: https://linkinghub.elsevier.com/retrieve/pii/S003039921630055X
[34] Q. Li, Y. Wang, H. Liu, X. He, D. Xu, J. Wang, and F. Guo, "Leukocyte cells identification and quantitative morphometry based on molecular hyperspectral imaging technology," *Comput. Med. Imag. Graph.*, vol. 38, no. 3, pp. 171–178, Apr. 2014. [Online]. Available: https://linkinghub.elsevier.com/retrieve/pii/S089561111300205X
[35] J. M. Bioucas-Dias, A. Plaza, N. Dobigeon, M. Parente, Q. Du, P. Gader, and J. Chanussot, "Hyperspectral unmixing overview: Geometrical, statistical, and sparse regression-based approaches," *IEEE J. Sel. Topics Appl. Earth Observ. Remote Sens.*, vol. 5, no. 2, pp. 354–379, Apr. 2012.

SAMUEL ORTEGA received the Telecommunication Engineering degree and the Research Master's degree in telecommunication technologies from the University of Las Palmas de Gran Canaria, Spain, in 2015 and 2016, respectively. In 2015, he started to work as a Coordination Assistant and a Researcher in the HELICoiD European Project, cofunded by the European Commission. Since then, he has conducted his research activity in the Integrated System Design Division, Institute for Applied Microelectronics, University of Las Palmas de Gran Canaria, in the field of electronic and bioengineering. His current research interest includes the use of machine learning algorithms in medical applications using hyperspectral images.

RAÚL GUERRA was born in Las Palmas de Gran Canaria, Spain, in 1988. He received the Industrial Engineering degree from the University of Las Palmas de Gran Canaria, in 2012, the master's degree in telecommunications technologies imparted from the Institute for Applied Microelectronics, IUMA, in 2013, and the Ph.D. degree in telecommunications technologies from the University of Las Palmas de Gran Canaria, in 2017. He was funded by the Institute of Applied Microelectronics to do his Ph.D. research with the Integrated System Design Division. In 2016, he was a Researcher with the Configurable Computing Lab, Virginia Tech University. His current research interests include the parallelization of algorithms for multispectral and hyperspectral images processing and hardware implementation.

MARÍA DÍAZ was born in Spain, in 1990. She received the Industrial Engineering degree from the University of Las Palmas de Gran Canaria, Spain, in 2014, and the master's degree in system and control engineering imparted jointly by the Universidad Complutense de Madrid and the Universidad Nacional de Educación a Distancia (UNED). She is currently pursuing the Ph.D. degree with the University of Las Palmas de Gran Canaria, developing her research activities at the Integrated Systems Design Division of the Institute for Applied Microelectronics (IUMA). In 2017, she conducted a research stay in the GIPSA-lab, University of Grenoble Alpes, France. Her research interests include image and video processing, development of highly parallelized algorithms for hyperspectral images processing, and hardware implementation.

HIMAR FABELO received the Telecommunication Engineering and the master's and Ph.D. degrees in telecommunication technologies from the University of Las Palmas de Gran Canaria, Las Palmas de Gran Canaria, Spain, in 2013, 2014, and 2019, respectively. In 2015, he started to work as a Coordination Assistant and a Researcher in the HELICoiD European Project, cofunded by the European Commission. In 2018, he performs a research stay in the Department of Bioengineering within the Erik Jonsson School of Engineering and Computer Science, The University of Texas at Dallas, collaborating with Prof. Baowei Fei in the use of medical hyperspectral imaging analysis using deep learning. Since then, he has conducted his research activity in the Integrated System Design Division, Institute for Applied Microelectronics, University of Las Palmas de Gran Canaria, in the field of electronic and bioengineering. His research interests include the use of machine learning and deep learning techniques applied to hyperspectral images to discriminate between healthy and tumor samples for human brain tissues in real-time during neurosurgical operations.

SEBASTIÁN LÓPEZ (M'08–SM'15) was born in Las Palmas de Gran Canaria, Spain, in 1978. He received the Electronic Engineering degree from the University of La Laguna, San Cristobal de La Laguna, Spain, in 2001, and the Ph.D. degree in electronic engineering from the University of Las Palmas de Gran Canaria, Las Palmas de Gran Canaria, in 2006.

He is currently an Associate Professor with the University of Las Palmas de Gran Canaria, where he is involved in research activities with the Integrated Systems Design Division, Institute for Applied Microelectronics. He has coauthored more than 120 articles in international journals and conferences. His research interests include real-time hyperspectral imaging, reconfigurable architectures, high-performance computing systems, and image and video processing and compression. Dr. López was a recipient of regional and national awards during his electronic engineering degree. He also serves as an Active Reviewer for different JCR journals and as a Program Committee Member of a variety of reputed international conferences. Furthermore, he acted as one of the program chairs of the IEEE Workshop on Hyperspectral Image and Signal Processing: Evolution in Remote Sensing (WHISPERS) in its 2014 edition and of the SPIE Conference of High Performance Computing in Remote Sensing, from 2015 to 2018. He is also an Associate Editor of the IEEE JOURNAL OF SELECTED TOPICS IN APPLIED EARTH OBSERVATIONS AND REMOTE SENSING, MDPI *Remote Sensing*, and *Mathematical Problems in Engineering Journal*. He was an Associate Editor of the IEEE TRANSACTIONS ON CONSUMER ELECTRONICS, from 2008 to 2013. Moreover, he has been the Guest Editor of different special issues in JCR journals related with his research interests.

GUSTAVO M. CALLICÓ (M'08) received the M.S. degree (Hons.) in telecommunication engineering and the Ph.D. degree (Hons.) and the European Doctorate from the University of Las Palmas de Gran Canaria (ULPGC), in 1995 and 2003, respectively. In 1994, he joined the Institute for Applied Microelectronics (IUMA); from 2000 to 2001, he stayed at the Philips Research Laboratories (NatLab) in Eindhoven, The Netherlands, as a Visiting Scientist, where he developed his Ph.D. thesis. From 1996 to 1997, he was granted with a Research Grant from the National Educational Ministry, in 1997, he was hired by the University as an Electronic Lecturer. He was an Invited Professor with the University of Pavia, Italy, from October 2015 to March 2019. He is currently an Associate Professor with the ULPGC. He also develops his research activities in the Integrated Systems Design Division, Institute for Applied Microelectronics (IUMA). He has more than 170 publications in national and international journals, conferences, and book chapters. He has participated in 18 research projects funded by the European Community, the Spanish Government, and international private industries. His current research interests include hyperspectral imaging for real-time cancer detection (brain, skin, and cervix), real-time super-resolution algorithms, synthesis-based design for SOCs, and circuits for multimedia processing and video coding standards, and especially for H.264 and SVC. Since 2015, he has been responsible for the scientific-technological equipment project called ''Hyperspectral image acquisition system of high spatial and spectral definition,'' granted by the General Directorate of Research and Management of the National Research and Development Plan, funded through the General Directorate of Scientific Infrastructure. He has been the Coordinator of the European project HELICoiD [FET (Future and Emerging Technologies)] under the Seventh Framework Program with grant. He has been an Associate Editor of the IEEE TRANSACTIONS ON CONSUMER ELECTRONICS, since 2009; he is also a Senior Associate Editor of this Journal. Additionally, he has been also an Associate Editor of IEEE ACCESS, since 2016.

ROBERTO SARMIENTO was a Visiting Professor with The University of Adelaida, South Australia, and later at the University of Edith Cowan, also in Australia, in 1993. He contributed to set this school up; he was the Dean of the Faculty, from 1994 to 1995, and a Vice-Chancellor for Academic Affairs and a Staff with the ULPGC, from 1998 to 2003. He is currently a Full Professor with the Telecommunication Engineering School, University of Las Palmas de Gran Canaria, Spain, in the area of electronic engineering. He is also a Founder of the Research Institute for Applied Microelectronics (IUMA) and the Director of the Integrated Systems Design Division of this Institute. Since 1990, he has published more than 50 journal articles and book chapters and more than 140 conference papers. He has been awarded with four six years research periods by the National Agency for the Research Activity Evaluation, Spain. He has participated in more than 45 projects and research programmes funded by public and private organizations, from which he has been a Lead Researcher in 16 of them. Between these projects, it has special mention those funded by the European Union, such as GARDEN and the GRASS workgroup and funded by the European Spatial Agency TRPAO8032. He has got several agreements with companies for the design of high performance integrated circuits, where the most important are those performed with Vitesse Semiconductor Corporation, California, Ensilica Ltd., U.K., and Thales Alenia Space, Spain.